

# Investigating Solid-State NMR Recoupling Sequences

U1608399

*Department of Physics, University of Warwick,  
Coventry, CV4 7AL, United Kingdom*

(Dated: December 13, 2021)

Nitrogen-Hydrogen correlation spectra are invaluable in solid-state magic angle spinning (MAS) NMR as nitrogen environments are often key to intermolecular hydrogen bonding which determine how molecules pack in e.g. pharmaceuticals. Whilst most NMR is done on the 0.4% natural abundance spin  $\frac{1}{2}$   $^{15}\text{N}$  isotope, this project considers the 99.6% natural abundance spin 1  $^{14}\text{N}$  isotope where there is the complication of the quadrupolar interaction. Two implementations of the  $^{14}\text{N}-^1\text{H}$  Heteronuclear Multiple Quantum Correlation (HMQC) approach are investigate: Dipolar HMQC (D-HMQC) based on rotary resonance recoupling ( $R^3$ ) methods, where the  $^1\text{H}$  nutation frequency is set to twice the MAS frequency, and TRAnsfer of Populations in DOuble Resonance HMQC (TRAPDOR-HMQC). Experiments are presented for the dipeptide,  $\beta$ -Aspartyl Alanine ( $\beta$ -AspAla) containing two nitrogen sites: NH and  $\text{NH}_3$  (with a large and small quadrupolar coupling respectively) at a MAS frequency of 50 kHz for a  $^1\text{H}$  Larmor frequency of 500 MHz. Experimental results are complemented by density matrix simulations using SIMPSON to investigate optimum recoupling times, nutation frequencies and pulse duration for both sequences. Experimental and simulated results indicate that the symmetry based, rotary resonance, SR4 $^2_1$  recoupling method in D-HMQC provides the best signal intensity in both nitrogen environments for 100 kHz  $^1\text{H}$  nutation frequency for a recoupling period of 10 rotor periods,  $\tau_R$ . T-HMQC produces the best sensitivity for an offset of 50 kHz for longer pulsing duration on  $^{14}\text{N}$  but is not as sensitive as SR4 $^2_1$  for the same parameters.

## I. INTRODUCTION

Nuclear Magnetic Resonance (NMR) spectroscopy utilises the intrinsic property of nuclear spin for the analysis of chemical and physical structures of various ma-

terials; it has developed over the last 75 years as a valuable analytical technique with applications in a vast range of sciences and industries [1–4]. One of the more notable applications of NMR is to

the pharmaceuticals field where most active pharmaceutical ingredients (APIs) are provided in solid form. Here, solid-state NMR spectroscopy, which allows for the observation of interactions that may not be present in solution state [5], is utilised in understanding the properties of these APIs that cannot all be explored with traditional solution-state methods [6, 7]. Nitrogen plays an important role in many of these API formulations, being involved in structural hydrogen-bonding and solid-state NMR provides a probe to allow us to determine how molecules pack together. Nitrogen has two isotopes, both these nuclei are spin active,  $^{14}\text{N}$  and  $^{15}\text{N}$ .  $^{14}\text{N}$  has an abundance of 99.6% however it has a lower gyromagnetic ratio and it is quadrupolar, making it a difficult nucleus to observe directly [8, 9]. Therefore, it is necessary to explore methods for the acquisition of  $^{14}\text{N}$  spectra indirectly and develop ways to optimise these methods where possible [10].

In this report, the indirect detection of  $^{14}\text{N}$  via protons is explored through the use of  $^{14}\text{N}-^1\text{H}$  Dipolar-Heteronuclear Multiple Quantum Correction (D-HMQC) [10–12] and TRAnsfer of Populations in DOuble Resonance HMQC (TRAPDOR- or T-HMQC) [13–15] at a fast magic angle spinning (MAS) frequency [16] of 50 kHz with a  $^1\text{H}$  Larmor frequency of 500 MHz for a sample of the dipeptide,  $\beta$ -AspAla. A range of

recoupling sequences  $\text{R}^3$ , SPI- $\text{R}^3$  and  $\text{SR4}_1^2$  [17–21] along with TRAPDOR have been implemented and optimised in order to produce the greatest sensitivity.

## II. THE FUNDAMENTALS OF NMR

### II.A. Spin, $B_0$ , Energy and Resonance

The behaviour of a nucleus of an atom is largely governed by its local chemical environment and through the observation of this behaviour, it is possible to build an understanding of the local environment and, by extension, the local structure of the substance under study. In this section, the theory needed to understand some of the behaviours of nuclear spin is explored. Much of this is based on theory that is found in [22–25].

Nuclei have an intrinsic angular momentum called spin angular momentum which can be considered a vector quantity,  $\mathbf{I}$ , where its magnitude is:

$$|\mathbf{I}| = \hbar\sqrt{I(I+1)}. \quad (1)$$

Here,  $I$  is the spin quantum number with possible values:  $\frac{1}{2}, 1, \frac{3}{2}, 2, \dots$  and in this report,  $^1\text{H}$  of spin  $\frac{1}{2}$  and  $^{14}\text{N}$  of spin 1 are investigated.

Due to its quantum nature, we can only know the value of  $\mathbf{I}$  projected onto a particular axis, for example, the  $z$ -axis:

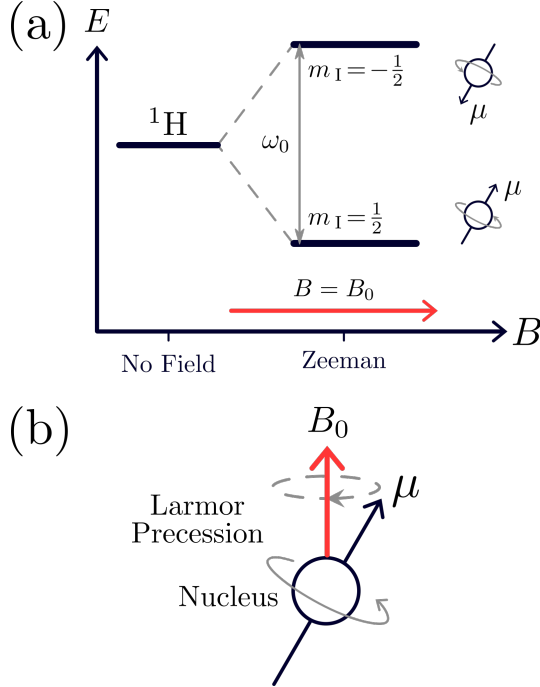


FIG. 1. (a) Schematic of the energy level splitting in the presence of an external magnetic field for a spin  $\frac{1}{2}$   $^1\text{H}$  nucleus going from the left,  $\mathbf{B} = 0$ , to the right,  $\mathbf{B} = \mathbf{B}_0$ . (b) Schematic of the Larmor precession of a magnetic moment,  $\mu$ , about an external magnetic field,  $B_0$ .

$$I_z = m_I \hbar, \quad (2)$$

where  $m_I$  is known as the magnetic quantum number with  $2I+1$  possible values; for a spin  $\frac{1}{2}$  nucleus like  $^1\text{H}$ ,  $m_I$  takes the values  $\pm\frac{1}{2}$ . We also need to consider the spin angular momentum of a nucleus, which is related to the magnetic moment,  $\mu$ , via the following relationship:

$$\mu = \gamma I, \quad (3)$$

where  $\gamma$  is the gyromagnetic ratio of that particular nucleus and can take positive or negative values.

The spin system is a quantum mechanical system and thereby has energy levels associated with its nuclear spin. Without

any magnetic field applied, the spin system is in a non-excited state which means it has  $m_I = 2I+1$  degenerate energy levels. However, once an external magnetic field,  $\mathbf{B}_0$ , along the  $z$ -axis, is applied, this degeneracy is lifted. The energy levels split into as many degenerate levels as there are in the nucleus (two here for a spin  $\frac{1}{2}$  nucleus), as shown by Figure 1(a). This is known as Zeeman splitting. The energy,  $E$ , experienced by the magnetic moments is proportional to the external field,  $\mathbf{B}_0$  and by applying equations (2) and (3) for components along the  $z$ -axis, we arrive at:

$$E = -\gamma m_I \hbar B_0, \quad (4)$$

where  $B_0$  is the magnitude of  $\mathbf{B}_0$  along the  $z$ -axis. In NMR, allowed transitions between energy levels occur only for the selection rule,  $\Delta m_I = \pm 1$ , therefore the energy difference between the energy levels is  $\Delta E = |\gamma| \hbar B_0$ . However, the difference in energy is also proportional to  $\omega_0 \hbar$ , thus:

$$\omega_0 = -\gamma B_0, \quad (5)$$

where, when in resonance,  $\omega_0$ , is the Larmor frequency which is defined the frequency of a magnetic moment when an external field is applied. It is to be noted that the actual field that is experienced is not the but  $\mathbf{B}_0$  it is  $\mathbf{B}_z$  as will be explained in section 1.E. The effect of this on a nucleus is shown in Figure 1(b). Typical magnetic field strengths used in exper-

iments currently range from 12 Tesla (like the one used for this report, corresponding to a  $^1\text{H}$  Larmor frequency of 500 MHz) to 28 Tesla (currently the strongest field in a NMR magnet, installed at the University of Florence in 2020, corresponding to a  $^1\text{H}$  Larmor frequency of 1.2 GHz)

When the system is at thermal equilibrium, the relative population difference known as the polarisation,  $P$ , between the number of spins aligned,  $N^+$ , and anti-aligned,  $N^-$ , with  $\mathbf{B}_0$  is explained via Boltzmann statistics:

$$\frac{N^+}{N^-} = e^{\frac{\Delta E}{k_B T}}, \quad (6)$$

where  $k_B$  is the Boltzmann constant,  $T$  is the absolute temperature and  $\Delta E$  represents the energy difference between the split states shown in Figure 1(a). The probability of a nucleus transitioning from the ground state to an excited state, or the excited state back down to the ground state is equal when an electromagnetic (EM) field's energy is absorbed. However, the difference in the total energy absorbed depends on the initial difference in the population of the two energy levels. There is a larger proportion of upward transitions compared to downward transitions, for example in a 11.75 Tesla magnet (as the one used for this report) at room temperature this is one part in around 10000. The sum of an ensemble of the induced magnetic moments (i.e. magnetic moments induced due to  $\mathbf{B}_0$ )

per unit volume is defined as the bulk magnetisation,  $\mathbf{M}$ , which points along  $\mathbf{B}_0$ . The comparably small difference in number of the upward transition explains why NMR is, by its nature, an insensitive technique. This therefore drives the focus on developing methods for increasing sensitivity, some of these are discussed in this report.

## II.B. $B_1$ and the Rotating Frame

In order for the magnetic resonance to be observed, the magnetisation needs to be moved away from its equilibrium position. This is done by applying a second magnetic field,  $\mathbf{B}_1$ , which is orthogonal to  $\mathbf{B}_0$ . This  $\mathbf{B}_1$  field is produced from a transmitter coil in which the sample is placed and an oscillating EM wave, typically in the radio frequency (RF) range with frequency  $\omega_{\text{RF}}$ , is applied, consequently,  $\mathbf{B}_1$  is also referred as the RF pulse which is applied as an os-

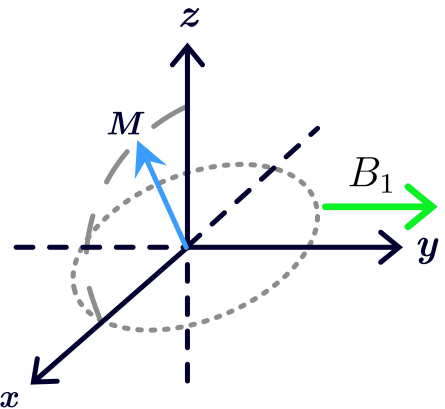


FIG. 2. Schematic representing the simplified vector model of the magnetisation tilting due to an RF pulse applied along the  $y$ -axis in the rotating frame.

cillating field represented by:

$$\mathbf{B}_1 = |\mathbf{B}_1| \cos(\omega_{\text{RF}} t + \phi), \quad (7)$$

where  $\omega_{\text{RF}} t$  is the flip angle of the magnetisation and  $\phi$  is the phase. Switching from the laboratory frame to the rotating frame simplifies this considerably. Here, the system rotates about  $\mathbf{B}_0$  at an angular frequency,  $\omega_{\text{RF}}$ .

If  $\omega_{\text{RF}}$  is equal to  $\omega_0$ , i.e. an on-resonance pulse is applied the magnetisation,  $\mathbf{M}$ , is tilted onto the transverse plane as shown by Figure 2. The on-resonance condition is met when the resonance offset,  $\Omega$ , is zero ( $\Omega = 0$  kHz).

When  $\mathbf{M}$  is in the transverse plane, it rotates around  $\mathbf{B}_1$  at the nutation frequency,  $\omega_1$ , and has the relationship:

$$\omega_1 = \gamma B_1. \quad (8)$$

It is to be noted that in the rotating frame,  $\mathbf{B}_1$  as a stationary field and the previously stationary  $\mathbf{B}_0$  becomes the reduced field,  $\Delta B_0$ , which is related to the offset,  $\Omega$ , via:

$$\Omega = \omega_0 - \omega_{\text{RF}} = -\gamma \Delta B_0. \quad (9)$$

Therefore for an on-resonance pulse, the reduced field is zero as such, the effective magnetic field,  $\mathbf{B}_{\text{eff}}$ , felt by the nuclei points in the same direction as  $\mathbf{B}_1$ .

After the RF pulse is removed,  $\mathbf{M}$  spirals back along its equilibrium position as its transverse components diminish, during a time  $t_2$ , and its longitudinal components increase back again during a time  $t_1$ .

Throughout this spiraling motion,  $\mathbf{M}$  cuts the transmitter coil (which now acts as a receiver coil) which in turn induces a current (via Lenz's Law) that is detected as the free induction decay (FID) signal by the spectrometer (an FID is a decaying sinusoidal wave). This signal is detected in the rotating frame and a Fourier transform of this produces an NMR spectra in the frequency domain. However, before the FIDs are produced, it is unknown in which direction (represented by the sign of the offset) the magnetisation is processing. This is understood using quadrature detection where the  $x$  and  $y$  components of the magnetisation (which are  $\frac{\pi}{2}$  out of phase) are mixed. The sign of the offset is determined from the resultant real (in phase) and imaginary (out of phase) FIDs. The Fourier transforms of these produces a real and imaginary spectrum.

### II.C. 2D NMR

For a traditional one-dimensional (1D) NMR experiment, RF pulses are applied to excite the system and the resulting FID signal is recorded almost immediately after. These are then Fourier transformed to produce a spectrum showing the signal intensity against the chemical shift (or frequency) as shown in Figure 3. However, in cases where overlapping peaks are produced or more than one interaction be-

tween spins needs to be observed, other multidimensional technique are used. For the purposes of this report, 2D NMR experiments have been performed.

A 2D NMR experiment consists of four stages as shown in Figure 3: Preparation, evolution, mixing and detection. The preparation stage is where a RF pulse is applied (including relevant increment delays) to produce the magnetisation on the indirectly observed nuclei. Then during the evolution stage, this magnetisation evolves for a time period  $t_1$ . The mixing stage is then required to allow for the evolved mag-

netisation to be detected. Finally the detection stage is where the signal is acquired during a time  $t_2$ . The signal from the evolution of the magnetisation is recorded for a range of increments of  $t_1$ ,  $\Delta t_1$ , from e.g. zero,  $\Delta t_1$ ,  $2\Delta t_1$ , ..., till however many increments are needed in order to produce the required array of FIDs. These are then Fourier transformed to produce a 2D NMR spectrum with two frequency dimensions corresponding to the direct ( $F_2$ , shown on the top) and indirect ( $F_1$ , shown on the side) dimensions respectively; the signal intensity is displayed as a contour plot.

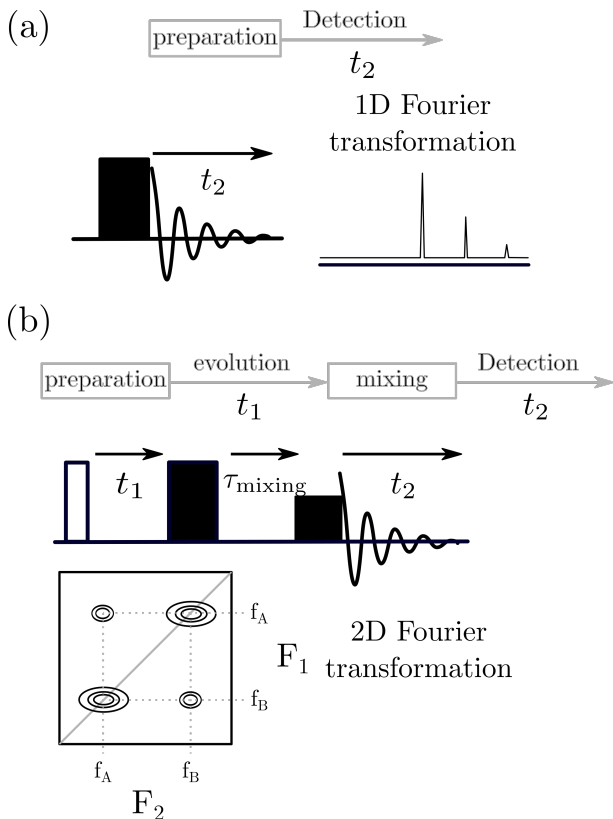


FIG. 3. Schematic representing NMR experiments for a (a) 1D pulse-acquire sequence and a (b) 2D EXSY (exchange spectroscopy) experiment [25]. This Figure has been adapted from [26].

## II.D. The Schrödinger Equation and the Density Operator

The simplified picture of the vector model outlined is unable to explain many of the phenomena that is observed, therefore a quantum mechanical description is required. The time dependent Schrödinger equation (TDSE) is central to this (with natural units  $\hbar = 1$ ):

$$\frac{d}{dt} |\Psi\rangle = -i\hat{H} |\Psi\rangle, \quad (10)$$

where  $|\Psi\rangle$  is the wavefunction of the system (sometimes called the state vector) and  $\hat{H}$  is the Hamiltonian operator (which corresponds to the measurable observable, energy). Equation (10) outlines the evolution of the wavefunction of the system under the Hamiltonian of that system. Solving

this equation produces the density operator which in turn allows us to understand the product operator formalism that will be discussed in due course.

First considering free precessional motion for the general initial state of a two-level system such as that of a spin  $\frac{1}{2}$  proton in  ${}^1\text{H}$  (represented in Figure 1(a)), where the wavefunction is a linear combination of the eigenfunctions of the Hamiltonian,  $|\alpha\rangle$  (spin up) and  $|\beta\rangle$  (spin down):

$$|\Psi\rangle = c_\alpha |\alpha\rangle + c_\beta |\beta\rangle, \quad (11)$$

where  $c_\alpha$  and  $c_\beta$  are complex and chosen such that the wavefunction is normalised.

In the vector model, the magnetisation vector was influenced by the magnetic fields, but in the quantum mechanical sense, the wavefunction of the system is influenced by its local environment which in turn is affected by the corresponding Hamiltonian that it evolves under.

In the general case, the expectation value of an operator,  $\hat{A}$  is:

$$\langle \hat{A} \rangle = \langle \Psi | \hat{A} | \Psi \rangle. \quad (12)$$

The expectation value of the Hamiltonian, (which is a Hermitian operator) has an observable relating to the energy,  $E$ . This along with, equations (2 – 4), it is possible to deduce the Hamiltonian under free precession in the rotating frame (known as the Zeeman Hamiltonian in the rotating frame):

$$\hat{H}_{\text{free}} = \Omega \hat{I}_z. \quad (13)$$

Thus,  $|\alpha\rangle$  and  $|\beta\rangle$  are equally the eigenfunctions of  $\hat{I}_z$  with their respective eigenvalues,  $m_l = \pm 1$ . from which it is possible to produce the eigenvalue equations:

$$\hat{I}_z |i\rangle = m_l |i\rangle, \quad (14)$$

for  $i = \alpha$  and  $\beta$ ; it is the same for  $\hat{I}_x$  and  $\hat{I}_y$ . Consequently, the expectation values of the three components of spin angular momentum are:

$$\langle \hat{I}_z \rangle = \frac{1}{2} c_\alpha^* c_\alpha - \frac{1}{2} c_\beta^* c_\beta, \quad (15)$$

$$\langle \hat{I}_x \rangle = \frac{1}{2} c_\alpha^* c_\beta + \frac{1}{2} c_\beta^* c_\alpha, \quad (16)$$

$$\langle \hat{I}_y \rangle = \frac{1}{2} i c_\beta^* c_\alpha - \frac{1}{2} i c_\alpha^* c_\beta, \quad (17)$$

where  $c_i^*$  denotes the complex conjugate of  $c_i$ . Equations (15) - (17) suggest that, e.g. for the  $z$ -component, each individual measurement of the spins produce a result of either  $\frac{1}{2}$  or  $-\frac{1}{2}$  but when a large number of measurements are performed, the average component of  $z$  is either  $\frac{1}{2}$ , with probability  $c_\alpha^* c_\alpha$ , or  $-\frac{1}{2}$  with probability,  $c_\beta^* c_\beta$ .

Now, considering the TDSE, (10) and substituting the superposition of states into the TDSE, then multiplying by  $\langle \alpha |$  and then  $\langle \beta |$  and integrating the respective results over all space, we get the following:

$$c_\alpha(t) = c_\alpha(0) e^{-i\Omega t/2}, \quad (18)$$

$$c_\beta(t) = c_\beta(0) e^{i\Omega t/2}. \quad (19)$$

Substituting these variables into those in equations (15 - 17), it is clear that  $\langle \hat{I}_z \rangle(t)$  is unchanged during free precession, however:

$$\langle \hat{I}_x \rangle \rightarrow \cos(\Omega t) \langle \hat{I}_x \rangle - \sin(\Omega t) \langle \hat{I}_y \rangle \quad (20)$$

$$\langle \hat{I}_y \rangle \rightarrow \cos(\Omega t) \langle \hat{I}_y \rangle + \sin(\Omega t) \langle \hat{I}_x \rangle \quad (21)$$

where the arrows represent the passage of time. This result is also produced from the vector models and also the density operator formalism which is introduced in a later section.

As has been discussed, the radio frequency pulse rotates the magnetisation onto the transverse plane, shown by Figure 2 and the Hamiltonian in the rotating frame (known as the RF Hamiltonian in the rotating frame) for an on resonance pulse about the  $x$ -axis is:

$$\hat{H}_{\text{pulse}} = \omega_1 \hat{I}_x. \quad (22)$$

Now we will analyse the effect of this Hamiltonian on the superposition state, we solve the TDSE as before but here, the rate of change of  $c_\alpha$  depends on  $c_\beta$  and vice versa ( $\langle \hat{I}_z \rangle$  is unchanged), but:

$$\langle \hat{I}_z \rangle \rightarrow \cos(\omega_1 t) \langle \hat{I}_z \rangle + \sin(\omega_1 t) \langle \hat{I}_y \rangle \quad (23)$$

$$\langle \hat{I}_y \rangle \rightarrow \cos(\omega_1 t) \langle \hat{I}_y \rangle + \sin(\omega_1 t) \langle \hat{I}_z \rangle \quad (24)$$

this, once again is as we expected from the vector model. Formally this description is what leads onto the product operator formalism.

## II.E. The Density Operator

The process described above can be done faster via matrix arithmetic if we introduce the concept of the density operator. The density operator can be described as

$$\hat{\rho} = |\Psi\rangle \langle \Psi|. \quad (25)$$

Thus, using the TDSE, (10), we can differentiate this to understand how  $\hat{\rho}$  evolves under a given Hamiltonian. Doing this produces yet another central equation to understanding NMR, the Liouville-von Neumann equation:

$$\frac{d\hat{\rho}}{dt} = -i[\hat{H}, \hat{\rho}], \quad (26)$$

where the Hamiltonian can take values including that described in (13) and (22). The solution to this differential equation is key in the product operator formalism and is given by:

$$\hat{\rho} = e^{-i\hat{H}\tau} \hat{\rho}(0) e^{i\hat{H}\tau}, \quad (27)$$

where  $\hat{\rho}(0)$  and  $\hat{\rho}(t)$  are the density operators at the start,  $t = 0$ , and at the time,  $t = \tau$ .  $\hat{H}$  is the Hamiltonian operator for the pulse sequence.

It is also important to consider the effect of ensemble averaging where macroscopic systems are composed of microscopic systems which develop independently, with different starting states, under the same Hamiltonian. Taking the example of two microscopic systems with initial states  $|\Psi_1\rangle$  and  $|\Psi_2\rangle$  respectively, here we would need

to calculate the behaviour of each system independently since you cannot sum the two states. The same issue arises when we consider density operators but it is simplified if it is only required to determine sum of the expectation values of  $|\Psi_1\rangle$  and  $|\Psi_2\rangle$  but not their the individual expectation values. Therefore, here the following expression is formed:

$$\langle \hat{A} \rangle_1 + \langle \hat{A} \rangle_2 = \text{Tr}([\rho_1 + \rho_2] \mathbf{A}) \quad (28)$$

where Tr is the trace of the argument. It is more convenient for the average of the density operators of the microscopic systems to be used in calculations, therefore, the density operator of an entire ensemble of microscopic systems, i.e. the macroscopic system, is the average of the density operators of these individual microscopic systems. This project uses a simulation package called SIMPSON [27] which essentially implements the time evolution of the density operator and the trace using the Hamiltonians discussed.

Product operators offer a simplified approach to understand how a coupled system evolves even though they are more suited where weak interactions are prevalent, namely J-coupling (details of which will be explained in the following section). Start by considering a two spin system where the nuclear spins labeled as  $I$  and  $S$ . The effect of pulsing on  $I$  (which initially in thermal equilibrium pointed along

the  $z$ -axis therefore labelled  $I_z$ ) about the  $x$ -axis by a flip angle,  $\theta$ , the magnetisation is effected as followed:

$$I_z \xrightarrow{\theta x} \cos(\theta)I_x - \sin(\theta)I_y. \quad (29)$$

Applying ideas from the vector model, equation (29) seems shows the magnetisation tilted by an angle  $\theta$  from the  $z$ -axis in the  $z - y$  plane. Also, letting the magnetisation evolve under an offset for some time,  $t$ , can be described as (ignoring  $I_z$  for the time being):

$$\begin{aligned} -\sin(\theta)(I_y) &\xrightarrow{\Omega t} -\sin(\theta)(\cos(\Omega t)I_y \\ &\quad - \sin(\Omega t)I_x). \end{aligned} \quad (30)$$

For the evolution between weakly coupled spins if, for example, the magnetisation is initially on  $I_x$ , then evolution under a J-coupling will be as followed:

$$\begin{aligned} I_x &\xrightarrow{\pi J_{IST}} \cos(\pi J_{IST})I_x \\ &\quad - \sin(\pi J_{IST})2I_yS_z. \end{aligned} \quad (31)$$

This equation shows that the magnetisation from  $I_x$  is transferred onto the  $2I_yS_z$ , therefore describing how the magnetisation evolves in time. In equation (31) the magnetisation has evolved from initially only being on spin  $I$  to now being on both spin  $I$  and spin  $S$ . Therefore magnetisation has been transferred.

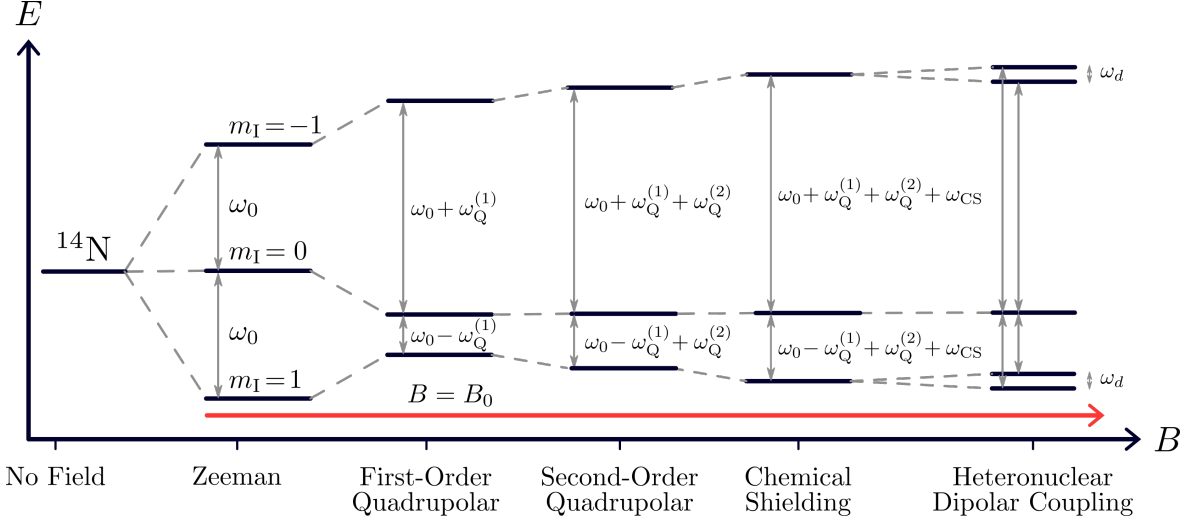


FIG. 4. Schematic of the energy level splitting in the presence of an external magnetic field of a  $^{14}\text{N}$  nucleus due to the interactions labeled. This Figure has been adapted from [9]

### II.F. Interactions

The Zeeman and RF Hamiltonians in the rotating frame have been introduced above. In this section the dependencies of other Hamiltonians relevant to this report are discussed.

It is understood that Zeeman splitting occurs due to the interaction of the nuclear spin with  $\mathbf{B}_0$  therefore, it is an example of an external interaction. There are other interactions (external and internal) in NMR but the Zeeman interaction is sufficiently strong that the others may be considered first order perturbations to it. This consideration is known as the secular approximation:

$$\hat{H} = \hat{H}_o + \hat{H}_1. \quad (32)$$

where  $\hat{H}_o$  is the Zeeman Hamiltonian and  $\hat{H}_1$  is the Hamiltonian for first order perturbation to  $\hat{H}_o$ .  $\hat{H}_1$  represents the sum Hamiltonians of the other interactions:

$$\hat{H}_1 = \hat{H}_{\text{RF}} + \hat{H}_{\text{CS}} + \hat{H}_{\text{D}} + \hat{H}_{\text{Q}} + \hat{H}_{\text{J}}. \quad (33)$$

where  $\hat{H}_{\text{RF}}$  is the Hamiltonian due to  $\mathbf{B}_1$  applied at the frequency  $\omega_{\text{RF}}$  as has been discussed above.  $\hat{H}_{\text{CS}}$ ,  $\hat{H}_{\text{D}}$ ,  $\hat{H}_{\text{Q}}$  and  $\hat{H}_{\text{J}}$  are the Chemical Shielding, Dipolar, Quadrupolar and J-coupling Hamiltonians respectively. Figure 4 illustrates the energy splitting due to some of these interactions in a  $^{14}\text{N}$  nucleus spinning at a fast MAS. Some of these interactions are explored below.

The chemical shift interaction is the result of electromagnetic induction where the external magnetic field forces a current to flow within the electron orbitals which, in turn, induces a local magnetic field. This has the effect of diminishing the experience magnetic field from  $\mathbf{B}_0$  to the effective field,  $\mathbf{B}_z$ :

$$\mathbf{B}_z = (1 - \sigma)\mathbf{B}_0 \quad (34)$$

where  $\delta$  is known as the shielding (or

screening) constant, thus the resonance frequency is shifted to:

$$|\omega_0| = |\gamma(1 - \sigma)\mathbf{B}_0|, \quad (35)$$

i.e. the Larmor frequency has shifted slightly to that introduced in section 1.A. Since each element, and by extension, each compound would have a unique electronic environment, this chemical shielding allows for the categorisation of each nucleus by its chemical fingerprint. Thus defining the chemical shift as the difference between the Larmor frequency of the nucleus of interest and that of a reference nucleus,  $\omega_{0\text{ref}}$ , the following relationship is reached:

$$\delta = \frac{\omega_0 - \omega_{0\text{ref}}}{\omega_{0\text{ref}}} \times 10^6. \quad (36)$$

where  $\delta$  is the chemical shift, the value of which is quoted in parts per million or ppm. This accounts for resonances produced due to different magnetic field strengths. However the shielding in a nucleus is orientationally dependant, i.e. interactions experienced along different molecular axes are not the same making it an anisotropic interaction. This is not a problem solution state NMR where the rapid tumbling of molecules cancels out any of these effects but in solid-state NMR, this is not averaged out. As will be explained later sections, this is removed in most solid state NMR methods via fast Magic Angle Spinning (this is similar for dipolar coupling, explained below).

Dipolar interactions (or dipolar couplings) is a through space interaction which arise when nuclei are close together; this allows for their own magnetic fields to interact with each other. Dipolar coupling is also anisotropic since it depends on the angle between the external field and the direction of the internuclear vector. In solid-state NMR this coupling is not averaged to zero like it is in solution-state NMR therefore solid-state NMR requires additional techniques to overcome this issue (as will be explained in Section 1.F. below). Without spinning at the fast frequencies at the so called magic angle, there is no doublet splitting. The dipolar coupling constant is given by the expression:

$$d = -\frac{\mu_0 \gamma_1 \gamma_2 \hbar}{4\pi r^3} \quad (37)$$

Quadrupolar coupling is also a prominent interaction in nuclei such as  $^{14}\text{N}$  (with  $I \geq 1$ ) have an electric quadrupole moment in addition to their magnetic dipole moment due to the non-uniform distribution of charge around the nucleus. The nuclear quadrupolar magnetic moment interacts with this non-uniform electric gradient field causing increased line broadening effects in the spectra. The quadrupolar coupling constant,  $C_Q$ , determines the strength of the coupling:

$$C_Q = \frac{e^2 q Q}{h} \quad (38)$$

where  $e$  is the electric charge,  $q$  is the elec-

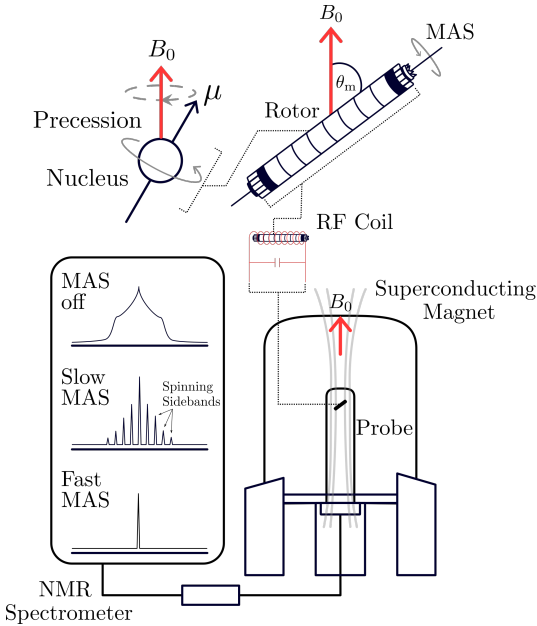


FIG. 5. The precession of a magnetic moment,  $\mu$ , about an external magnetic field,  $B_0$  at the Larmor frequency,  $\omega_0$ .  $\beta$ -AspAla is packed into a rotor which is positioned at the magic angle,  $\theta_m$ , relative to  $B_0$ . A coil of wire, capable of emitting and detecting RF radiation is wrapped around the rotor. This is all housed inside a probe which is placed inside a superconducting magnet. A static rotor produces a very broad signal but one spinning at fast MAS is able to produce a smaller linewidth from the NMR Spectrometer.

tric field gradient and  $Q$  is the nuclear quadrupolar moment.

Another interaction is J-coupling however, for the purposes of this report, this type of coupling is not considered in detail since there is not enough resolution to see the this splitting compared to the ones that follow.

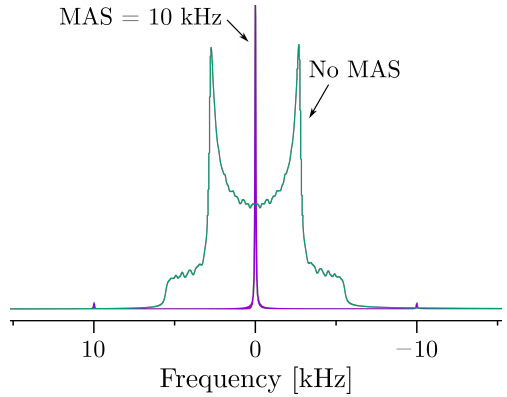


FIG. 6. Simulated lineshapes produced from the dipolar coupling between two heteronuclear spin  $\frac{1}{2}$  nuclei. The green lineshape is for a static (no MAS) condition and the purple lineshape corresponds to using 10 kHz MAS frequency.

## II.G. Solid State NMR Lineshapes and Magic Angle Spinning

Solid-state NMR spectra are generally significantly broader than those for solution-state NMR since there is no averaging of anisotropic interactions that arise in the (rigid) solid-state like there is in a liquid where the random tumbling of molecules average out these effects. Therefore the issue comes not from the absence of information, but rather spectra broadening encapsulates such a wealth of information that techniques have been developed to remove much of the details so that NMR phenomena can be studied in their isolation.

The key to achieving much of the line narrowing in solid state NMR spectra was found in solving the dipolar interaction term shown by the expression [28]:

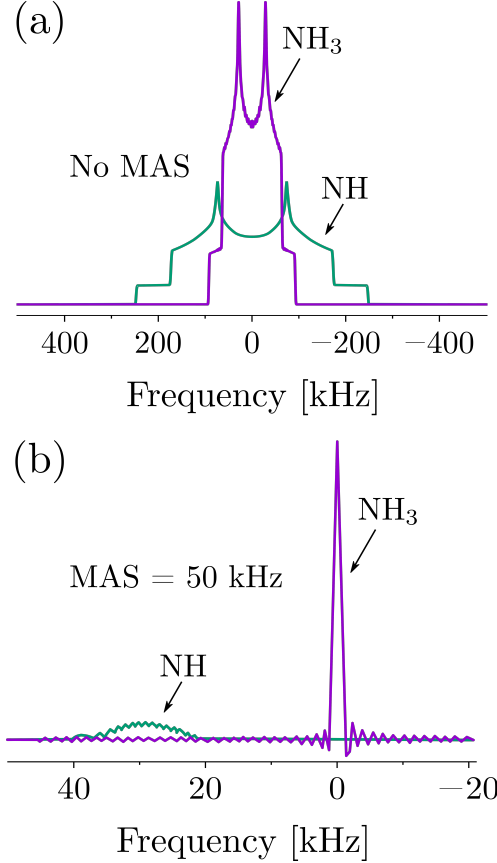


FIG. 7. Simulated lineshapes for  $C_Q = 1.23$  MHz (purple) and  $C_Q = 3.29$  MHz (green)  $^{14}\text{N}$  environments showing (a) a static (no MAS) condition and (b) MAS = 50 kHz.

$$D = d \left[ \frac{1}{2} (3 \cos^2(\beta) - 1) \right] \quad (39)$$

for the angle,  $\beta$ , one can determine the magic angle, of  $54.7^\circ$  with respect to the external magnetic field as shown by the rotor positioned at  $\theta_m$  in Figure 5 spinning at a fast magic angle frequency.

Spinning at the magic angle at high frequencies is referred to as fast Magic Angle Spinning. This has the effect of suppressing anisotropic chemical shift and dipolar interactions. Figures 6 and 7 illustrates the effect that MAS has in removing line broad-

ening caused by these isotropic interactions. However, Figure 7 shows that for nuclei with spin  $> 1$  such as  $^{14}\text{N}$ , the quadrupolar interaction produces very large spectral broadening. Even though fast MAS is able to remove first-order quadrupolar coupling, second-order quadrupolar coupling remains persistent.

However, as has been mentioned, MAS allows for line narrowing but at the cost of removing valuable information that interactions such as heteronuclear dipolar coupling hold about molecular structures. Therefore recoupling techniques are required to selectively reintroduce the desired interactions for further study. This is explained in the section that follows.

## II.H. HMQC and Recoupling

In this report, solid state 2D NMR experiments have been performed to optimise signal intensity from the correlation between nitrogen and hydrogen spins. More specifically, Heteronuclear Multiple Quantum Coherence (HMQC), experiments have been implemented where the chemical shifts of  $^1\text{H}$  and  $^{14}\text{N}$  are correlated and the peaks (called cross shifts) are produced due to heteronuclear dipolar coupling between the two nuclei. Here, in order to attain the greatest signal intensity, it is necessary to directly detect on the nucleus with the greatest  $\gamma$ .  $^1\text{H}$  has a large  $\gamma$  and conse-

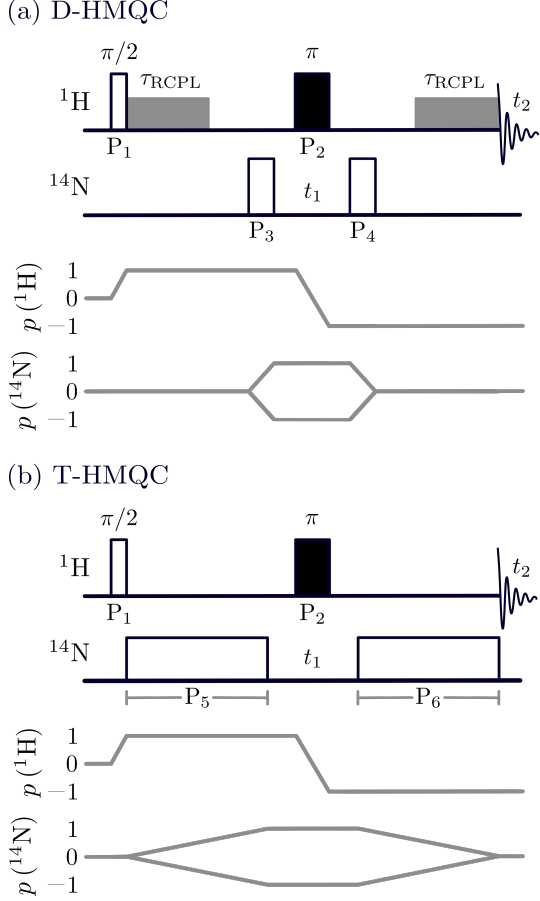


FIG. 8. Schematic representing the  $^{14}\text{N}$ - $^1\text{H}$  pulse sequence and coherence transfer pathways for (a) D-HMQC and (b) T-HMQC sequences. The various recoupling segments that were investigated are shown on the sequence as solid grey blocks.

quently a large  $\omega_0$  via equation (3). This in turn creates a larger  $\mu$  which induces a larger current in the RF coil which consequently produces a larger signal. Therefore the  $^1\text{H}$  nucleus (who's  $\gamma$ , relative to that of  $^{14}\text{N}$ , is a factor of fourteen times greater) is detected upon. In the context of a heteronuclear correlation experiment, with the  $^1\text{H}$  and  $^{14}\text{N}$  nuclear spins labeled as  $I$  and  $S$  respectively, during the evolution state, the dipolar coupling present between the two nuclei allows for the magnetisation to

be transferred from the  $I$  spin to the  $S$  spin. From Figure 8, the HMQC pulse sequence can be described as followed: initially, the magnetisation on the  $I$  spin is excited by a RF pulse. It then develops into an anti-phase state between  $P_1$  and  $P_3$ . After this,  $P_3$  turns this state into heteronuclear multiple quantum coherence. This evolves during  $t_1$  but it is then turned, once again, into in-phase  $I$  spin magnetisation and coupling between the  $I$  and  $S$  spin is able to rephase, which is then acquired during  $t_2$ . However, as has been explained in Section 2.E and 2.F above, MAS removes the dipolar couplings between nuclei therefore, in order to facilitate any magnetisation transfer, dipolar coupling must be reintroduced. This must, however, be reintroduced such that only heteronuclear coupling (e.g.  $^1\text{H}$ - $^{14}\text{N}$ ) is allowed but not homonuclear coupling (e.g.  $^1\text{H}$ - $^1\text{H}$ ). Therefore recoupling techniques such as the R-based:  $\text{R}^3$ , SPI- $\text{R}^3$  and  $\text{SR4}_1^2$  or alternative pulsing techniques such as TRAPDOR must be implemented to the HMQC pulse sequence. These recoupling techniques have been developed to combat the spectral broadening that the couplings outlined above produce.

In D-HMQC, the R-based recoupling techniques use used to pulse on the  $^1\text{H}$  channel at the rotary resonance condition,  $n=2$ , where the nutation frequency of  $^1\text{H}$  is set to twice the MAS frequency [17–21].

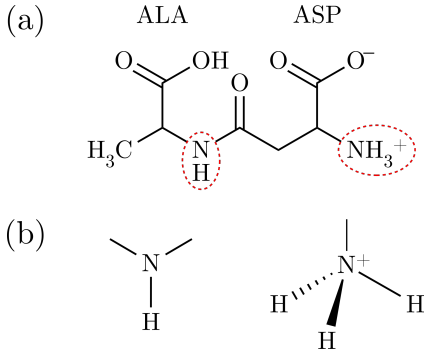


FIG. 9. (a) A schematic of  $\beta$ -AspAla and (b) a schematic of the  $\text{NH}$  and  $\text{NH}_3$  groups.

This reintroduces the heteronuclear dipolar coupling between the nuclei. The T-HMQC pulse sequence is different to D-HMQC in that here, there is no recoupling applied to the  $^1\text{H}$  channel but longer pulses are applied onto the  $^{14}\text{N}$  channel.

### III. EXPERIMENTAL DETAILS

#### III.A. Experiment

Solid-state NMR experiments were performed using a Bruker Avance III spectrometer, equipped with a 11.75 T superconducting magnet. A sample of  $\beta$ -AspAla was packed into a 1.3 mm rotor inside a HXY probe in double resonance mode at a MAS frequency of 50 kHz (unless otherwise stated) tuned to the  $^1\text{H}$  Larmor frequency of 500 MHz and the  $^{14}\text{N}$  Larmor frequency of 36.1 MHz.

The D-HMQC experiment consisted of a  $\frac{\pi}{2}$  pulse on the  $^1\text{H}$  channel of  $2.5 \mu\text{s}$  and a pulse on the  $^{14}\text{N}$  channel of  $9 \mu\text{s}$  with the  $^1\text{H}$  nutation frequency set to 100 kHz. 16

scans were co-added with a recycle delay of 2 s and  $48t_1$  FIDs were acquired for a total experimental time of 25 minutes and 36 seconds. The recoupling regimes,  $\text{R}^3$ , SPI- $\text{R}^3$ , and  $\text{SR4}_1^2$  were added in the  $^1\text{H}$  as shown by Figure 8 for a recoupling period of  $\tau_{\text{RCPL}}$ . The T-HMQC experiment used the same pulse times as in the D-HMQC experiment but the pulse duration on  $^{14}\text{N}$  was varied from  $5 \tau_{\text{R}}$  ( $100 \mu\text{s}$ ) to  $40 \tau_{\text{R}}$  ( $800 \mu\text{s}$ ). Spectra were recorded for  $^{14}\text{N}$  nutation frequencies of 40 kHz, 50 kHz and 60 kHz for 25 kHz and 50 kHz offset each time. The spectral reference frequency for  $^{14}\text{N}$  was found using the reference compound  $\text{NH}_4\text{Cl}$  at  $-341.2 \text{ ppm}$ . Bruker's own software, TopSpin was used to record and manipulate and plot spectra.

#### III.B. Simulation

Simulations have been performed using the simulation package, SIMPSON [27, 29, 30] which was used to simulate pulse sequences before implementing them on the spectrometer and, except where otherwise stated, the simulations are for a  $^{14}\text{N}-^1\text{H}$  spin pair. The magnitude of the dipolar coupling was taken to be 10 kHz (corresponding to a bond length of  $0.95\text{\AA}$ ). The  $C_Q$  for  $\text{NH}$  and  $\text{NH}_3$  are 3.29 MHz and 1.29 MHz respectively. The  $\eta_Q$  for  $\text{NH}$  and  $\text{NH}_3$  are 0.38 and 0.4 respectively. Both the  $C_Q$  and  $\eta_Q$  values are taken from the calculated GI-

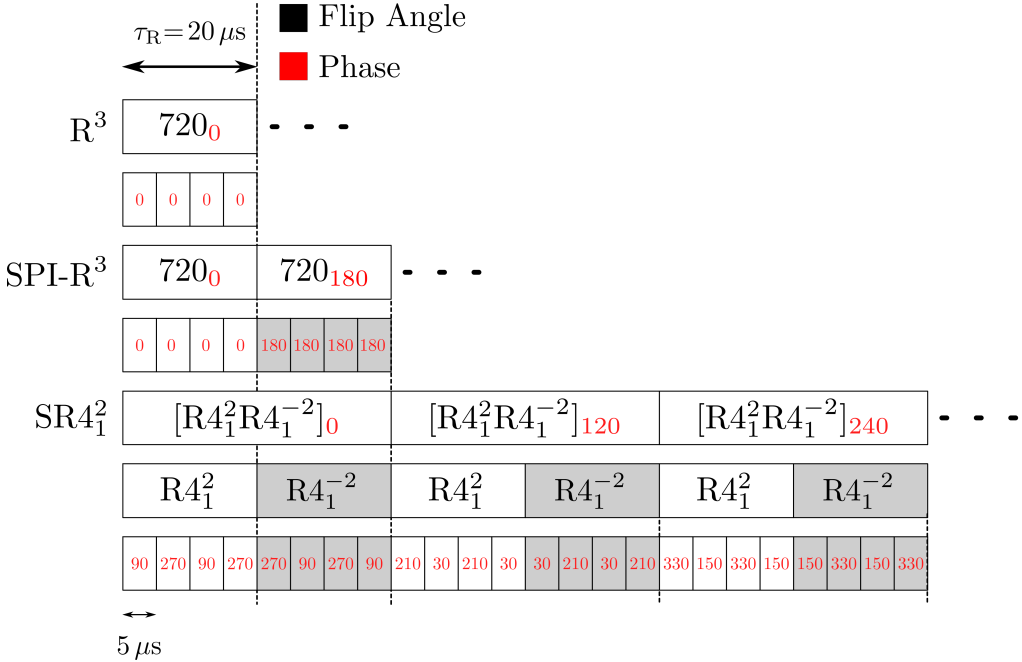


FIG. 10. A schematic showing the phases at 50 kHz MAS for (a)  $R^3$ , (b)  $SPI-R^3$  and (c)  $SR4_1^2$  recoupling sequences. Each quarter of a rotor cycle ( $5 \mu s$ ), the angle is flipped by  $180^\circ$  (hence  $720^\circ$  flipped every rotor cycle). The subscripts coloured red represents the phase.

PAW results in [12]. The simulations do not include the effects of spin relaxation.

#### IV. RESULTS AND DISCUSSION

##### IV.A. 1D Spectrum of $\beta$ -AspAla

Chemical structure and 1D spectrum representing environments in  $\beta$ -AspAla. The black line shows a one-pulse on the  $^1H$  dimension. The red and blue lines represent the 1D  $NH_3$  and  $NH$  spectra respectively, taken for  $SR4_1^2$  recoupling at  $40 \tau_R$  recoupling at 100 kHz  $^1H$  nutation frequency. The height of the one-pulse has been scaled to the intensity of the  $NH_3$  environment for illustration.

The dipeptide  $\beta$ -AspAla contains two chemically distinct nitrogen sites  $NH$  and

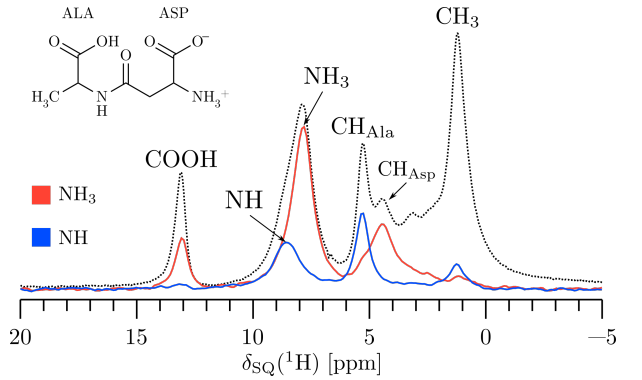


FIG. 11. 1D  $^1H$  (500 MHz, 50 kHz MAS) D-HMQC NMR spectrum of the dipeptide  $\beta$ -AspAla. The black dotted line shows a one-pulse. The red and blue lines represent the  $NH_3$  and  $NH$  1D spectra extracted from a 2D spectrum (see below) for  $SR4_1^2$  recoupling at  $40 \tau_R$  recoupling period at 100 kHz  $^1H$  nutation frequency. The height of the one-pulse has been scaled to the intensity of the  $NH_3$  environment for illustration.

$NH_3^+$  as seen in the structure in Figure 9. Figure 11 shows a 1D spectrum for the groups inside  $\beta$ -AspAla. Nearby pro-

ton environments along with bond distance measurements can be understood in terms of which peaks show where: the NH group is close in proximity [12] to the CH<sub>3</sub> and CH<sub>Ala</sub> groups. The NH<sub>3</sub> group is close in proximity to the COOH and CH<sub>Asp</sub> groups thus those peaks are seen for its spectra. Table I shows the assigned chemical shifts from Figure 11. As will be expanded upon below, this figure highlights that the recoupled heteronuclear dipolar interactions via SR4<sub>1</sub><sup>2</sup> recoupling provides the essential information to understand molecular structure.

In the following section, the effectiveness of the recoupling schemes, R<sup>3</sup>, SPI-R<sup>3</sup> and SR4<sub>1</sub><sup>2</sup> using the n=2 condition (the nutation frequency of <sup>1</sup>H is set to twice the MAS frequency) is compared to that of TRAPDOR recoupling where longer RF pulses are applied on the <sup>14</sup>N channel and optimum parameters for each experiment are discussed. The phase cycles used for the D-HMQC recoupling regimes are shown in Figure 10.

TABLE I. Experimental chemical shifts for the groups within  $\beta$ -AspAla taken for SR4<sub>1</sub><sup>2</sup> recoupling at 40  $\tau_R$  at 100 kHz <sup>1</sup>H nutation frequency (with an error of  $\pm 0.05$  ppm), taken from Figure 11.

Group	Chemical Shift, $\delta$ [ppm]
COOH	13.1
NH	8.6
NH <sub>3</sub>	7.8
CH <sub>Ala</sub>	5.3
CH <sub>Asp</sub>	4.5
CH <sub>3</sub>	1.2

#### IV.B. Dipolar-HMQC with R3-type Recoupling

The <sup>14</sup>N-<sup>1</sup>H (500 MHz, 50 kHz MAS) D-HMQC pulse sequence with the recoupling schemes R<sup>3</sup>, SPI-R<sup>3</sup> and SR4<sub>1</sub><sup>2</sup> are compared in Figure 12. A recoupling period,  $\tau_{RCPL}$ , of 10  $\tau_R$  (200  $\mu$ s) and a <sup>1</sup>H nutation frequency of 100 kHz has been used for all three recoupling regimes. All other experimental parameters were kept the same. The 2D spectra in this figure allow the distinct peaks for the NH and NH<sub>3</sub> environments in the indirect dimension to be observed. The significant advantage of 2D spectra is highlighted here since this is not seen for the 1D spectrum shown by the black dotted line in Figure 11 where only the <sup>1</sup>H environment is seen. Additionally, the indirect dimension showcases the effect of the quadrupolar interaction; the NH environment has greater line broadening and a lower intensity due to its greater  $C_Q$  as seen in equation (38) and Figure 7.

It is also clear from Figure 12 that R<sup>3</sup> recoupling produces the lowest signal to noise with the lowest peak intensities for both NH and NH<sub>3</sub> whereas the SPI-R<sup>3</sup> and SR4<sub>1</sub><sup>2</sup> schemes produced greater sensitivity. From this, it is suggestive that a constant phase applied for R<sup>3</sup> recoupling, as shown in Figure 10, doesn't provide sufficient excitation compared to a phase cycle with an alternating phase.

Figure 13 considers this in more detail. Here the extracted rows from 2D  $^{14}\text{N}-^1\text{H}$  (500 MHz, 50 kHz MAS) D-HMQC spectra for the two nitrogen environment are compared for different nutation frequencies and recoupling periods. The intensities are scaled to the maximum intensity for SR4 $^2_1$  at 100 kHz  $^1\text{H}$  nutation frequency for a recoupling time of  $20 \tau_R$  as shown in Figure 13(b).

Figure 13(a) and (c) shows the variation of the nutation frequency of  $^1\text{H}$  at a constant recoupling time of  $10 \tau_R$  for both nitrogen environments. The intensity of the peaks increases with the nutation frequency, producing a maximum at twice the spinning frequency. This is suggestive that the n=2 condition is being followed where only heteronuclear interactions are recoupled.

Figure 13(b) and (d) show the variation of the recoupling period of the R-based sequences for a constant  $^1\text{H}$  nutation frequency of 100 kHz for both nitrogen environments. There is much similarity between these figures and that shown in Figure 11. As explained earlier, in  $\beta$ -AspAla, the NH $_3$  and NH environments are surrounded by other groups, (see Figure 9). Therefore, not only is the one-bond correlation due to the NH and NH $_3$  environments seen, but peaks are also seen due to the longer range NH connectivities when re-

coupling is allowed for longer times. Thus, peaks are observed at different  $^1\text{H}$  chemical shifts as shown in Table I.

Now taking a closer look into this, in Figure 13(a) and (c), it is clear that SR4 $^2_1$  seems to be sensitive to nutation frequencies for environments with a greater quadrupole interaction, much more so than the other two R-based sequences as represented by the relatively low intensities between 92 kHz and 98 kHz but the stark jump at 100 kHz. This may be suggestive also of the fact that higher nutation frequencies should have been explored since there seems to be a discrepancy between experiment and simulation. SPI-R $^3$  on the other hand produces peaks which only show a maximum variation of 15% for the NH environment. This is contrary to what is shown by the simulation in Figure 14 that will be discussed below. Also, whilst it is clear that R $^3$  produces the lowest intensity peaks, it still seems to show less dependency on the nitrogen environment than SR4 $^2_1$ . Additionally, SPI-R $^3$  and SR4 $^2_1$  show peaks or longer range interactions in  $\beta$ -AspAla for greater nutation frequencies. However, since further nutation frequencies were not studied, this remains something that can be investigated in future work.

Figure 14 shows SIMPSON simulations for a  $^{14}\text{N}-^1\text{H}$  spin pair under the D-HMQC (500 MHz, 50 kHz MAS) pulse sequence for

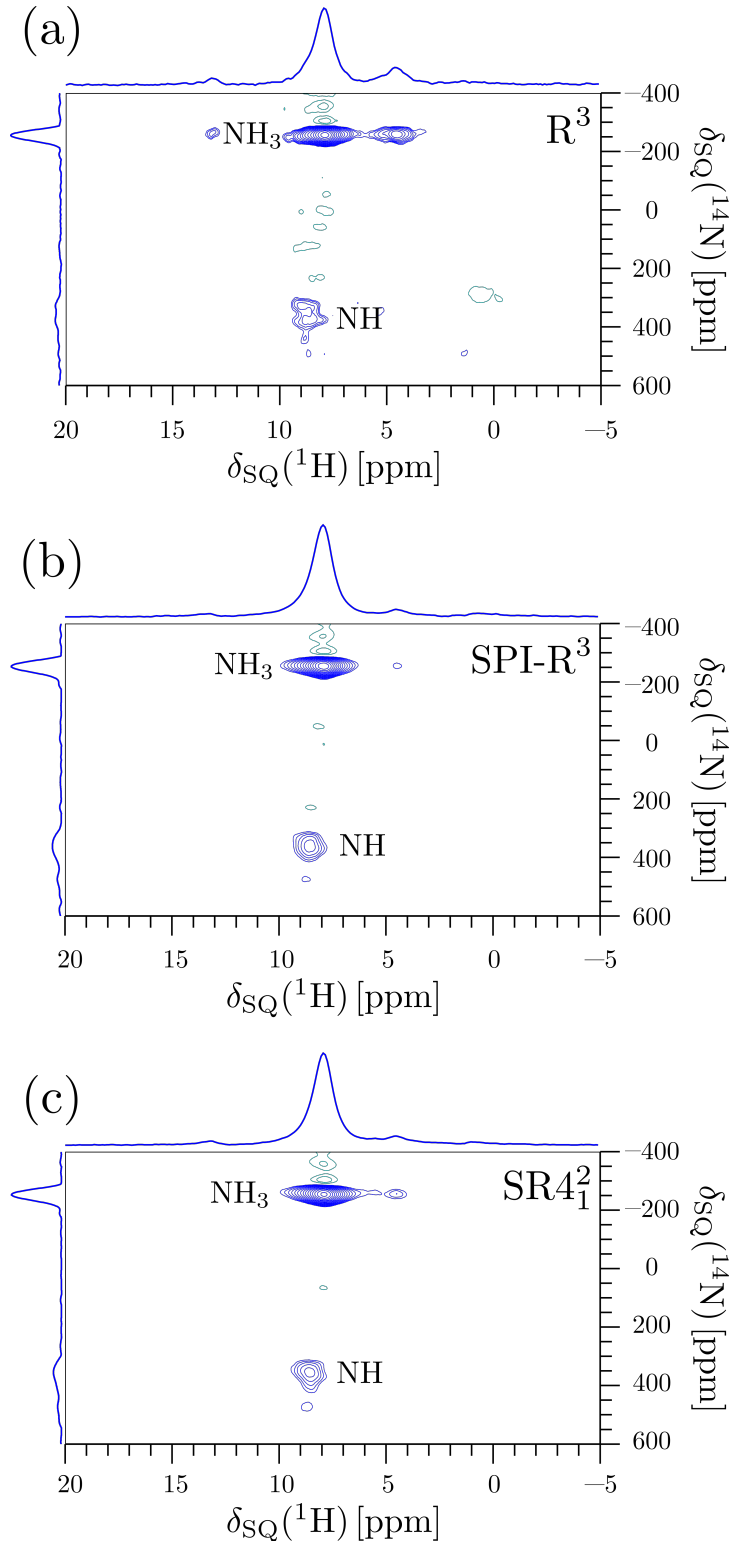


FIG. 12. Experimental  $^{14}\text{N}$ – $^1\text{H}$  (500 MHz, 50 kHz MAS) D-HMQC NMR spectra with skyline projections of the dipeptide  $\beta$ -AspAla recorded with  $\tau_{\text{RCPL}} = 10 \tau_R$  (200  $\mu\text{s}$ ) at 100 kHz  $^1\text{H}$  nutation frequency for recoupling regimes using the  $n = 2$  condition: (a)  $R^3$ , (b) SPI- $R^3$  and, (c)  $\text{SR}4_1^2$ . All spectra were recorded with the same number of  $t_1$  FIDs and total experimental time. The  $^1\text{H}$  transmitter frequency was set to -1.53 ppm. The base contours are at (a) 7%, (b) 8% and, (c) 6% of the maximum peak heights.

the recoupling regimes R<sup>3</sup>, SPI-R<sup>3</sup> SR4<sub>1</sub><sup>2</sup>. Here the intensity is relative to a one-pulse experiment. These simulations complement the experimental spectra shown in Figures 12 and 13 in that Figure 14(a) and (c) confirms that a nutation frequency at twice the MAS frequency (the n=2 condition) produces the highest signal intensity. Also, whilst experimental spectra in shows similar intensity between SPI-R<sup>3</sup> SR4<sub>1</sub><sup>2</sup> near the n=2 condition, it is not nearly as close as that shown here. This indicates that whilst the simulations are robust, they do not entirely represent what actually occurs.

It is clear that greater recoupling times favour the NH<sub>3</sub> environment, however a recoupling time of 10  $\tau_R$  produced the most intensity for the NH environment for SPI-R<sup>3</sup> and SR4<sub>1</sub><sup>2</sup>. These results are in agreement with the simulations in Figure 14(b) and (d) which show that recoupling periods around 10  $\tau_R$  is optimum whereas recoupling the NH<sub>3</sub> environment shows greater intensity for larger recoupling periods.

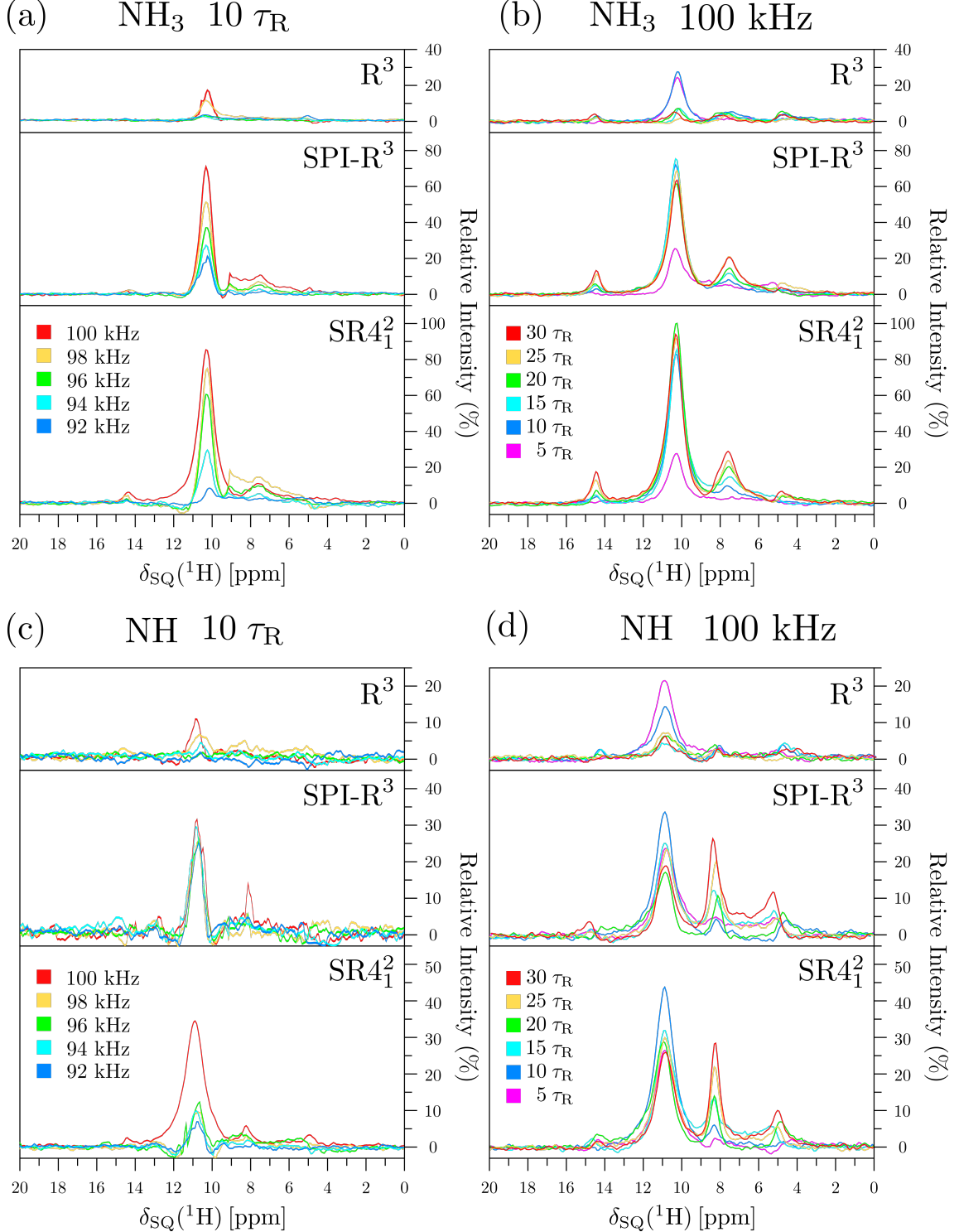


FIG. 13. Experimental data extracted from spectra for the  $\text{NH}_3$  and  $\text{NH}$  nitrogen resonances of the dipeptide  $\beta$ -AspAla for the D-HMQC (500 MHz, 50 kHz MAS) pulse sequence for  $R^3$ ,  $\text{SPI}-R^3$  and  $\text{SR}4_1^2$  recoupling regimes for (a)  $^1\text{H}$  nutation frequencies from 70 kHz to 100 kHz, (b) recoupling periods (in units of rotor periods) from 5  $\tau_R$  to 20  $\tau_R$ , (c)  $\text{NH}$  nitrogen resonances for (c)  $^1\text{H}$  nutation frequencies from 70 kHz to 100 kHz and (d) recoupling periods (in units of rotor periods) from 5  $\tau_R$  to 20  $\tau_R$ . The extracted data correspond to the sum of the extract rows from -380 ppm to -123 ppm and from 230 ppm to 500 ppm for the  $\text{NH}_3$  and  $\text{NH}$  environments respectively. The  $^1\text{H}$  transmitter frequency was set to -1.53 ppm. The intensities are scaled to the maximum intensity for D-HMQC,  $\text{SR}4_1^2$  at 100 kHz  $^1\text{H}$  nutation frequency for a recoupling time of 20  $\tau_R$  as shown in (b).

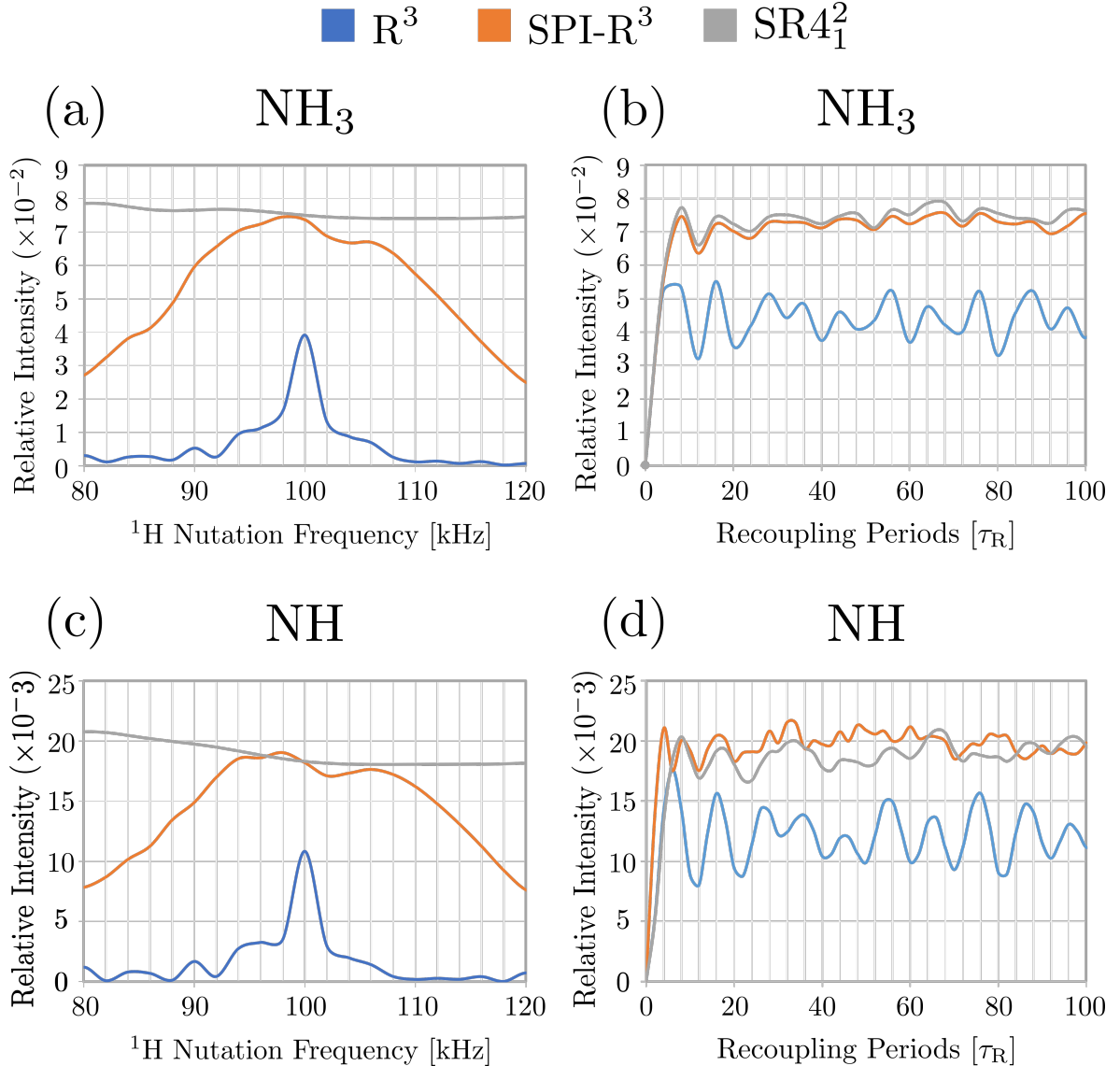


FIG. 14. Simulated data (using SIMPSON) for a  $^{14}\text{N}$ - $^1\text{H}$  spin pair under the D-HMQC (500 MHz, 50 kHz MAS) pulse sequence for the recoupling regimes  $\text{R}^3$ , SPI- $\text{R}^3$  SR4 $_1^2$ . The intensity is relative to a one-pulse experiment. The change of intensity against the nutation frequencies is shown for the (a) NH<sub>3</sub>, (c) NH, and the recoupling periods for (b) NH<sub>3</sub> (d) NH. The  $C_Q$  of NH<sub>3</sub> and NH were set to 1.23 MHz and 3.29 MHz respectively. The  $\eta_Q$  of NH<sub>3</sub> and NH were set to 0.38 and 0.4 respectively. The pulse length on the  $^{14}\text{N}$  was 2.5  $\mu\text{s}$  and the dipolar coupling was set to 10 kHz.

#### IV.C. TRAPDOR-HMQC

The  $^{14}\text{N}-^1\text{H}$  (500 MHz, 50 kHz MAS) T-HMQC pulse sequence recouples heteronuclear interactions by applying long RF pulses on the  $^{14}\text{N}$  channel; its spectra is shown in Figure 15. Here  $^{14}\text{N}$  RF pulse offsets of 40 kHz, 50 kHz and 60 kHz are investigated for two different  $^{14}\text{N}$  nutation frequencies, 25 kHz and 50 kHz. The  $^1\text{H}$  nutation frequency has been kept constant at 50 kHz.

Figure 15 shows that varying the offset from 40 kHz to 60 kHz produces a change in the intensity of the nitrogen environment, indicating that T-HMQC has a dependence on the  $^{14}\text{N}$  pulse offset, in agreement with that shown in [31]. The  $^{14}\text{N}$  nutation frequency shows a significant dependence on the excitation of the NH environment; a harder pulse produces greater signal intensity.

Figure 16 compares the signal intensity produced from the T-HMQC and D-HMQC (using SR4<sub>1</sub><sup>2</sup> recoupling) pulse sequences for recoupling times ranging from  $5 \tau_R$  to  $40 \tau_R$  in both the  $\text{NH}_3$  and NH environments. Here it is shown that a  $^{14}\text{N}$  RF pulse duration of  $40 \tau_R$  produces a comparable intensity to SR4<sub>1</sub><sup>2</sup> for a recoupling period of  $5 \tau_R$ . Also, the longer range peaks (showing the contributions of the longer range NH connectivities in  $\beta$ -AspAla) are not seen in Figure 16(a) which is more akin

to R<sup>3</sup> shown in Figure 13.

Figures 14 and 18 show SIMPSON simulations for a  $^{14}\text{N}-^1\text{H}$  spin pair in a T-HMQC (500 MHz, 50 kHz MAS) pulse sequence.

In Figure 14, the intensities, relative to a one-pulse experiment, are plotted against the  $^{14}\text{N}$  pulse length in rotor periods,  $\tau_R$ , for the NH and  $\text{NH}_3$  nitrogen environments. It is clear that the intensity in both environments increases with the recoupling period. This confirms what is seen in the Figure 16.

Figure 18 shows the intensity, relative to a one-pulse experiment, against three different  $^{14}\text{N}$  pulse offset, 25 kHz 50 kHz and 10 kHz for a  $^{14}\text{N}$  nutation frequency of 50 kHz. It is clear that pulsing at a  $^{14}\text{N}$  offset of 50 kHz produces the highest signal intensity but an on-resonance pulse produces almost zero intensity.

Looking closer at 16, it is clear that for the same amount of recoupling applied, SR4<sub>1</sub><sup>2</sup> is the superior technique. However, the T-HMQC produces a smaller signal to noise ratio compared to the D-HMQC, recoupling sequences at similar peak intensities as can also be seen by the contour levels for Figure 12 compared to Figure 15(b), suggesting that, in-fact T-HMQC is a more efficient method; something that was also confirmed in [31]. To explore this further, experiments with longer RF duration would be required.

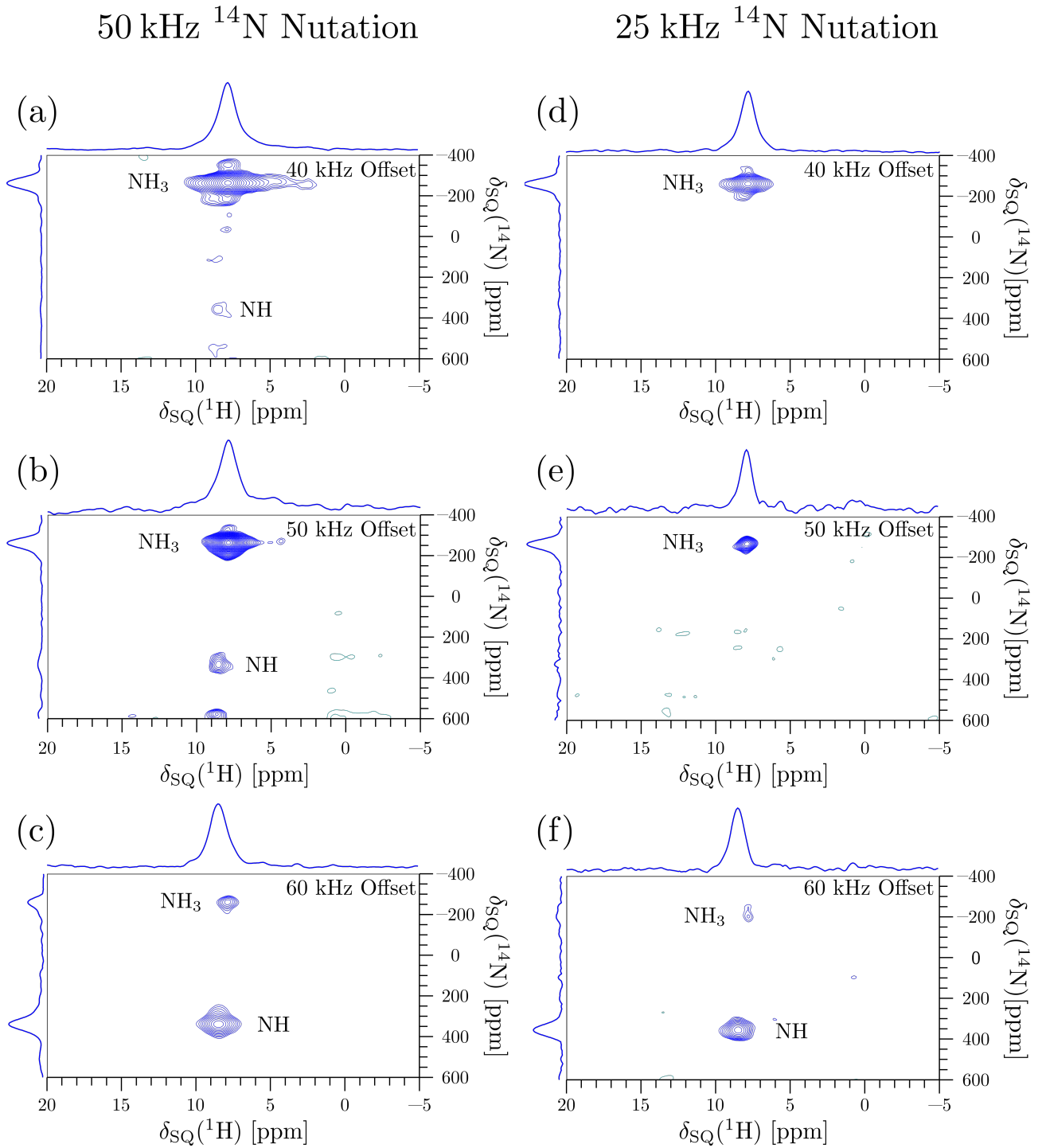


FIG. 15. Experimental  $^{14}\text{N}$ - $^1\text{H}$  (500 MHz, 50 kHz MAS) T-HMQC NMR spectra with skyline projections of the dipeptide  $\beta$ -AspAla with a  $^{14}\text{N}$  pulse length of  $20 \tau_{\text{R}}$  ( $600 \mu\text{s}$ ) at 50 kHz  $^1\text{H}$  nutation frequency. 50 kHz (a)-(c) and 25 kHz (d)-(f)  $^{14}\text{N}$  nutation frequencies at pulse offsets of (a,d) 40 kHz, (b,e) 50 kHz and (c,f) 60 kHz have been investigated. All spectra were recorded with the same number of  $t_1$  FIDs and total experimental time. The  $^1\text{H}$  transmitter frequency was set to -1.53 ppm. The base contours are at (a) 9%, (b) 4.5%, (c) 18%, (d) 30%, (e) 10% and (f) 17% of the maximum peak heights.

Also, comparing the simulations taken for longer recoupling duration in Figures 14 and 17, the intensity for SR4<sub>1</sub><sup>2</sup> approaches an envelope between  $7 \times 10^{-2}$  and  $8 \times 10^{-2}$  relative to the intensity of a one pulse however, T-HMQC does not show this behaviour; this indicates that T-HMQC can reach higher intensities than SR4<sub>1</sub><sup>2</sup> for much longer recoupling periods however, this once again remains something that can be investigated for future work.

Both sequences are rotor synchronised therefore, D-HMQC requires a frequency offset meaning it needs a first order phase correction. This leads to noise seen during the evolution under  $t_1$ . In contrast, T-HMQC does not need phase correction owing to the longer <sup>14</sup>N irradiation pulses. This explains why there is more efficient transfer of magnetisation in T-HMQC, thus explaining its better signal to noise ratio. Additionally, in Figure 16, the NH<sub>3</sub> environment shows a smooth increase of intensity for increase RF pulse duration whilst the NH environment does not; here the optimum RF duration seems to be  $15 \tau_R$ . This is in contrast to what is indicated by the simulation on Figure 17.

Finally, Figure 18 complements these results by giving further evidence for the offset dependency of T-HMQC. Applying the <sup>14</sup>N RF pulse at 50 kHz offset seems to excite a wide bandwidth which explains why

a greater intensity is seen in Figure 15(b) and is in agreement with what is shown by [31].

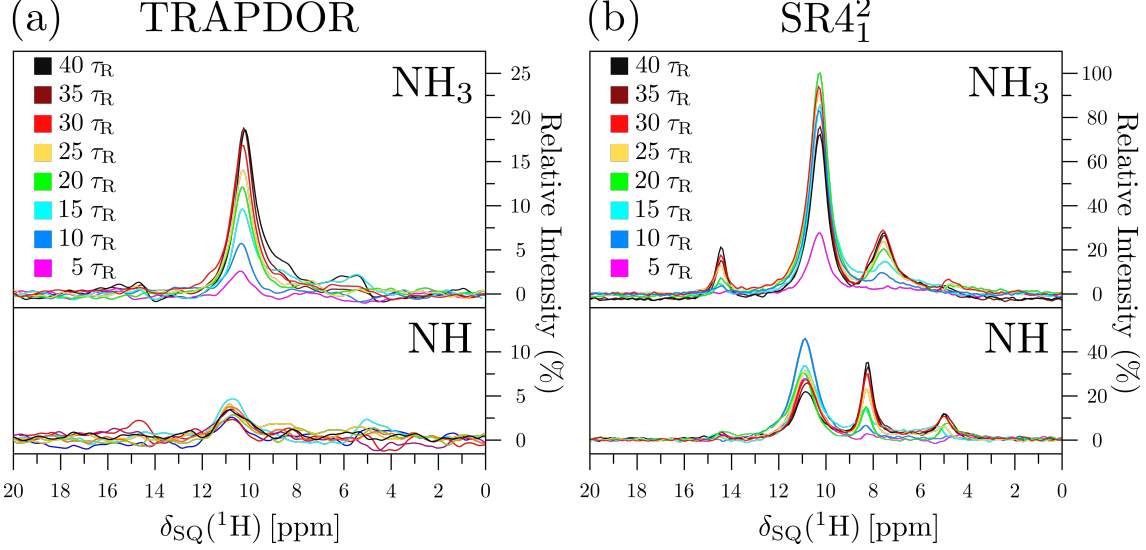


FIG. 16. Experimental data of the extracted rows from  $^{14}\text{N}-^1\text{H}$  (500 MHz, 50 kHz MAS) HMQC NMR spectra for the dipeptide  $\beta$ -AspAla for NH<sub>3</sub> and NH nitrogen resonances for (a)  $^{14}\text{N}$  pulse duration in rotor periods from 5  $\tau_R$  to 40  $\tau_R$ , at a  $^{14}\text{N}$  nutation frequency and pulse offset of 50 kHz, and (b) recoupling rotor periods for the SR4<sub>1</sub><sup>2</sup> from 5  $\tau_R$  to 40  $\tau_R$ , at a  $^1\text{H}$  nutation frequency of 100 kHz. The extracted data correspond to the sum of the extract rows from -380 ppm to -123 ppm and from 230 ppm to 500 ppm for the NH<sub>3</sub> and NH environments respectively. The  $^1\text{H}$  transmitter frequency was set to -1.53 ppm. The intensities are scaled to the maximum intensity for D-HMQC, SR4<sub>1</sub><sup>2</sup> at 100 kHz  $^1\text{H}$  nutation frequency for a recoupling time of 20  $\tau_R$  as shown in Figure 13 (b)

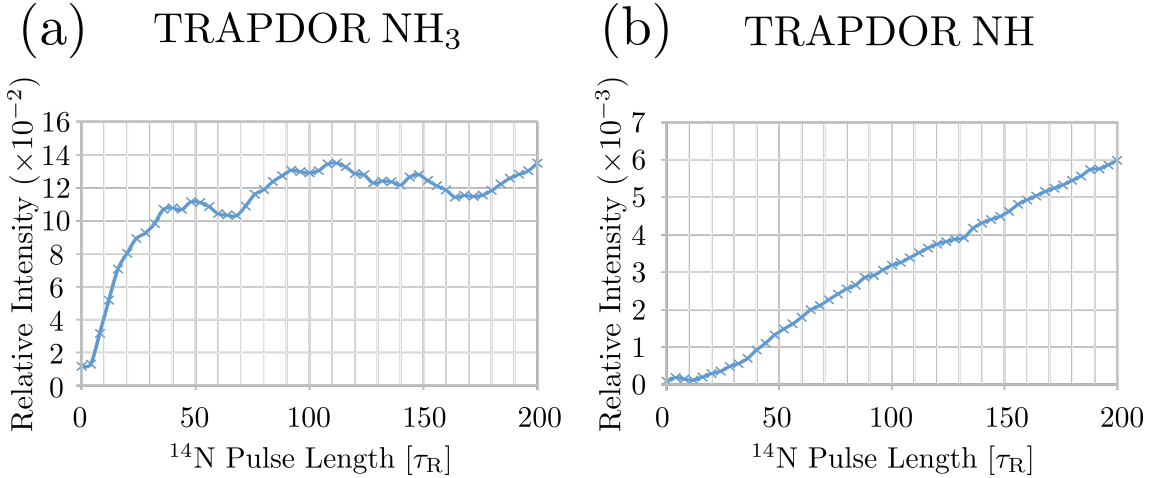


FIG. 17. Simulated data (USING SIMPSON) for a  $^{14}\text{N}-^1\text{H}$  spin pair in a T-HMQC (500 MHz, 50 kHz MAS) pulse sequence showing the intensity relative to a one-pulse experiment against the  $^{14}\text{N}$  pulse length in rotor periods,  $\tau_R$ , for the (a) NH<sub>3</sub> ( $C_Q = 1.18$  MHz) and (b) NH ( $C_Q = 3.29$  MHz) nitrogen environments. The  $C_Q$  of NH<sub>3</sub> and NH were set to 1.23 MHz and 3.29 MHz respectively. The  $\eta_Q$  of NH<sub>3</sub> and NH were set to 0.38 and 0.4 respectively. The dipolar coupling was set to 10 kHz.

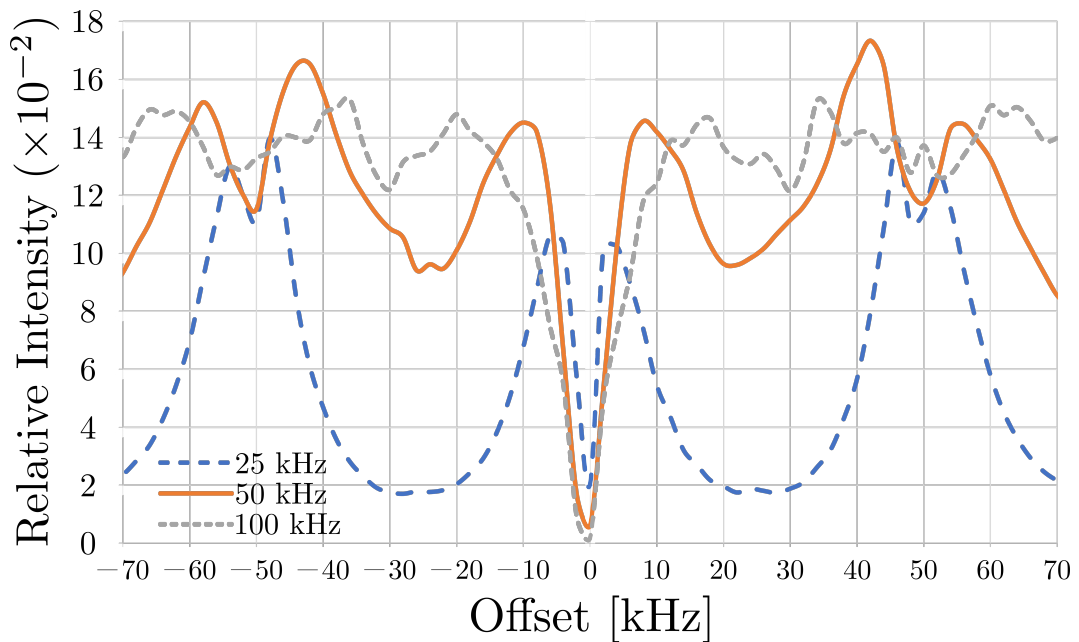


FIG. 18. Simulated data (using SIMPSON) for a  $^{14}\text{N}-^1\text{H}$  spin pair in a T-HMQC (500 MHz, 50 kHz MAS) pulse sequence showing the intensity relative to a one-pulse experiment against varying  $^{14}\text{N}$  nutation frequency offsets of 25 kHz (blue dashed line), 50 kHz (orange solid line) and 100 kHz (grey dashed line) for the  $\text{NH}_3$  nitrogen environment. The  $C_Q$  of  $\text{NH}_3$  and NH were set to 1.23 MHz and 3.29 MHz respectively. The  $\eta_Q$  of  $\text{NH}_3$  and NH were set to 0.38 and 0.4 respectively. The pulse length on the  $^{14}\text{N}$  was  $40 \tau_R$  and the dipolar coupling was set to 10 kHz.

## V. CONCLUSIONS AND OUTLOOK

It has been shown, through experimental and simulated data, that R<sup>3</sup>, SPI-R<sup>3</sup> and SR4<sub>1</sub><sup>2</sup> recoupling schemes produce the greatest signal intensity in the NH environment at a recoupling period of 10  $\tau_R$  and a <sup>1</sup>H nutation frequency of 100 KHz which is in agreement with the simulated data. It was also shown that SR4<sub>1</sub><sup>2</sup> produced the greatest signal intensity out of the three recoupling schemes, closely followed by SPI-R<sup>3</sup>. However, experiments suggest that SR4<sub>1</sub><sup>2</sup> is more sensitive to the change in nutation frequency compared to SPI-R<sup>3</sup> across both nitrogen environment. However, simulations showed the opposite; this may be due to the fact that the simulations are only for a two spin system and do not include the effects of multi-spin dephasing. Nevertheless, it offers a topic to investigate for future works. On the other hand, simulations agree well for the results where the recoupling period was varied. The NH<sub>3</sub> environment generally showed an increase in intensity for an increase in recoupling time whereas the NH environment showed that 10  $\tau_R$  was the optimum recoupling time.

The results from D-HMQC were compared against those from T-HMQC. This

recoupling method offers less recoupling of homonuclear interactions for a larger pulse duration, however this technique requires the offset to be set perfectly at the spinning sidebands and very long RF pulses to be applied on <sup>14</sup>N. For this report, the greatest intensities were produced for a <sup>14</sup>N offset of 50 kHz at a <sup>14</sup>N nutation frequency of 50 kHz, and although this was done for <sup>14</sup>N pulse length of 20  $\tau_R$ , simulations indicate this would only increase for greater recoupling times. This method agreed well with those found in [31] however, comparing SR4<sub>1</sub><sup>2</sup> and TRAPDOR recoupling, it is clear that for the same experimental recoupling and irradiation times of 10  $\tau_R$ , SR4<sub>1</sub><sup>2</sup> offers the greater sensitivity by a large margin.

In summary, the optimisation of the <sup>1</sup>H–<sup>14</sup>N MAS NMR pulse sequence, described in this report, provides valuable applications to e.g. pharmaceuticals where most APIs are provided in solid form. These APIs contain nitrogen which plays an important role in structural hydrogen bonding which determine how molecules pack. Therefore the methods presented in this report offer valuable insight to produce more sensitive <sup>1</sup>H–<sup>14</sup>N spectra which, through the probe that MAS NMR provides, allow for further study of these environments.

- 
- [1] B. Reif, S. E. Ashbrook, L. Emsley, and M. Hong, Solid-State NMR Spectroscopy, *Nat Rev Methods Primers.*, **1** (2021).
- [2] E. L. Drain, Principles and Applications of Nuclear Magnetic Resonance, *Br. J. Appl. Phys.*, **8**, S27 (1957).
- [3] E. D. Becker, A Brief History of Nuclear Magnetic Resonance, *Anal. Chem.*, **65**, 295A (1993).
- [4] L. F. Gladden, Industrial Applications of Nuclear Magnetic Resonance, *Chem. Eng. J. Biochem. Eng. J.*, **56**, 149 (1995).
- [5] S. P. Brown, Applications of High-Resolution  $^1\text{H}$  Solid-State NMR, *Solid State Nucl. Magn. Reson.*, **41**, 1 (2012).
- [6] M. Geppi, G. Mollica, S. Borsacchi, and C. A. Veracini, Solid-State NMR Studies of Pharmaceutical Systems, *Appl. Spectrosc. Rev.*, **43**, 202 (2008).
- [7] R. T. Berendt, D. M. Sperger, P. K. Isbester, and E. J. Munson, Solid-State NMR Spectroscopy in Pharmaceutical Research and Analysis, *Trends Analyt. Chem.*, **25**, 977 (2006).
- [8] S. L. Veinberg, K. E. Johnston, M. J. Jaroszewicz, B. M. Kispal, C. R. Mireault, T. Kobayashi, M. Pruski, and R. W. Schurko, Natural Abundance  $^{14}\text{N}$  and  $^{15}\text{N}$  Solid-State NMR of Pharmaceuticals and Their Polymorphs., *Phys. Chem. Chem. Phys.*, **18**, 17713 (2016).
- [9] L. A. O'Dell, Direct Detection of Nitrogen-14 in Solid-State NMR Spectroscopy, *Prog. Nucl. Mag. Res. Sp.*, **59**, 295 (2011).
- [10] A. G. M. Rankin, J. Trébosc, P. Paluch, O. Lafon, and J. P. Amoureaux, Evaluation of Excitation Schemes for Indirect Detection of  $^{14}\text{N}$  via Solid-State HMQC NMR Experiments, *J. Magn. Reson.*, **303**, 28 (2019).
- [11] P. K. Mandal and A. Majumdar, A Comprehensive Discussion of HSQC and HMQC Pulse Sequences, *Concepts. Magn. Reson.*, **20A**, 1 (2004).
- [12] A. S. Tatton, J. P. Bradley, D. Iuga, and S. P. Brown,  $^{14}\text{N}-^1\text{H}$  Heteronuclear Multiple-Quantum Correlation Magic-Angle Spinning NMR Spectroscopy of Organic Solids, *Z. Phys. Chem.*, **226**, 1187 (2012).
- [13] E. R. H. van Eck, R. Janssen, W. E. J. R. Maas, and W. S. Veeman, A Novel Application of Nuclear Spin-Echo Double-Resonance to Aluminophosphates and Aluminosilicates, *Chem. Phys. Lett.*, **174**, 428 (1990).
- [14] C. P. Grey, W. S. Veeman, and A. J. Vega, Rotational Echo  $^{14}\text{N}/\ ^{13}\text{C}/\ ^1\text{H}$  Triple Resonance Solid-State Nuclear Magnetic Resonance: A Probe of  $^{13}\text{C}-^{14}\text{N}$  Internuclear Distances, *J. Chem. Phys.*,

- 98**, 7711 (1993).
- [15] C. P. Grey and A. J. Vega, Determination of the Quadrupole Coupling Constant of the Invisible Aluminum Spins in Zeolite HY with  $^1\text{H}$ /  $^{27}\text{Al}$  TRAPDOR NMR, *J. Am. Chem. Soc.*, **117**, 8232 (1995).
- [16] E. R. Andrew, A. Bradbury, and R. G. Eades, Nuclear Magnetic Resonance Spectra from a Crystal Rotated at High Speed, *Nature.*, **182**, 1659 (1958).
- [17] Z. Gan, J. P. Amoureaux, and J. Trébosc, Proton-Detected  $^{14}\text{N}$  MAS NMR using Homonuclear Decoupled Rotary Resonance, *Chem. Phys. Lett.*, **435**, 163 (2007).
- [18] Z. Gan, Measuring Nitrogen Quadrupolar Coupling with  $^{13}\text{C}$  Detected Wide-Line  $^{14}\text{N}$  NMR under Magic-Angle Spinning, *Chem. Commun.*, **7**, 868 (2008).
- [19] A. Brinkmann and M. H. Levitt, Symmetry Principles in the Nuclear Magnetic Resonance of Spinning Solids: Heteronuclear Recoupling by Generalized Hartmann–Hahn Sequences, *J. Chem. Phys.* **115**, 357.
- [20] S. J. Huang, S. B. Liu, and J. C. C. Chan, Heteronuclear Dipolar Recoupling of Half-Integer Quadrupole Nuclei under Fast Magic Angle Spinning, *Solid State Nucl. Magn. Reson.*, **36**, 110 (2009).
- [21] N. T. Duong, F. Rossi, M. Makrinich, A. Goldbort, M. R. Chierotti, R. Go betto, and Y. Nishiyama, Accurate  $^1\text{H}$ - $^{14}\text{N}$  Distance Measurements by Phase-Modulated RESPDOR at Ultra-Fast MAS, *J. Magn. Reson.*, **308**, 106 (2019).
- [22] M. H. Levitt, *Spin Dynamics: Basics of Nuclear Magnetic Resonance*, 2nd ed. (John Wiley & Sons, Chichester, 2008).
- [23] J. Keeler, *Understanding NMR Spectroscopy* (John Wiley & Sons, Chichester, 2005).
- [24] P. J. Hore, *Nuclear Magnetic Resonance*, 2nd ed. (Oxford University Press, Oxford, 2015).
- [25] P. J. Hore, A. J. Jones, and S. Wimperis, *NMR: The Toolkit How Pulse Sequence Work*, 2nd ed. (Oxford University Press, Oxford, 2015).
- [26] A. Forse, *Nuclear Magnetic Resonance Studies of Ion Adsorption in Supercapacitor Electrodes [Unpublished doctoral thesis (2015)]* (University of Cambridge).
- [27] M. Bak, J. T. Rasmussen, and N. C. Nielsen, SIMPSON: A General Simulation Program for Solid-State NMR Spectroscopy, *J. Magn. Reson.*, **147**, 296 (2000).
- [28] E. R. Andrew, Magic Angle Spinning in Solid State NMR Spectroscopy, *Phil. Trans. R. Soc. Lond. A.*, **299**, 505 (1981).
- [29] Z. Tošner, R. Andersen, B. Stevensson, M. Edén, N. C. Nielsen, and T. Vosegaard, Computer-Intensive Simu-

- lation of Solid-State NMR Experiments Using SIMPSON, *J. Magn. Reson.*, **246**, 79 (2014).
- [30] Z. Tošner, T. Vosegaard, C. Kehlet, N. Khanej, S. J. Glaser, and N. C. Nielsen, Optimal Control in NMR Spectroscopy: Numerical Implementation in SIMPSON, *J. Magn. Reson.*, **197**, 120 (2009).
- [31] I. Hung, P. Gor'kov, and Z. Gan, Efficient and Sideband-Free  $^1\text{H}$ -Detected  $^{14}\text{N}$  Magic-Angle Spinning NMR, *J. Chem. Phys.*, **151**, 154 (2019).